Double layer charging driven carbon dioxide adsorption limits the rate of electrochemical carbon dioxide reduction on Gold

Ringe, Stefan; Morales-Guio, Carlos G.; Chen, Leanne D.; Fields, Meredith; Jaramillo, Thomas F.; Hahn, Christopher; Chan, Karen

Published in:
Nature Communications

Link to article, DOI:
10.1038/s41467-019-13777-z

Publication date:
2020

Document Version
Peer reviewed version

Double layer charging driven carbon dioxide adsorption limits the rate of electrochemical carbon dioxide reduction on Gold

Stefan Ringe [b),],[1,2,a)] Carlos G. Morales-Guio,[1,2,3,b)] Leanne D. Chen,[4] Meredith Fields,[1,2] Thomas F. Jaramillo,[1,2] Christopher Hahn,[1,2] and Karen Chan[5,c)]

[1)] *SUNCAT Center for Interface Science and Catalysis, Department of Chemical Engineering, Stanford University, Stanford, California 94305, United States*

[2)] *SUNCAT Center for Interface Science and Catalysis, SLAC National Accelerator Laboratory, Menlo Park, California, 94025, United States*

[3)] *Department of Chemical and Biomolecular Engineering, University of California, Los Angeles, CA 90095, United States*

[4)] *Division of Chemistry and Chemical Engineering, California Institute of Technology, Pasadena, CA 91125, USA*

[5)] *CatTheory Center, Department of Physics, Technical University of Denmark, Kongens Lyngby 2800, Denmark*

(Dated: 12 November 2019)

Abstract

Electrochemical CO_2 reduction is a potential route to the sustainable production of valuable fuels and chemicals. Here, we perform CO_2 reduction experiments on Gold at neutral to acidic pH values to elucidate the long-standing controversy surrounding the rate-limiting step. We find the CO production rate to be invariant with pH on a Standard Hydrogen Electrode scale and conclude that it is limited by the CO_2 adsorption step. We present a new multi-scale modeling scheme that integrates *ab initio* reaction kinetics with mass transport simulations, explicitly considering the charged *electric double layer*. The model reproduces the experimental CO polarization curve and reveals the rate-limiting step to be *COOH to *CO at low, CO_2 adsorption at intermediate, and CO_2 mass transport at high overpotentials. Finally, we show the Tafel slope to arise from the *CO_2-dipole-field interaction. In sum, this work highlights the importance of surface charging for electrochemical kinetics and mass transport.

Introduction

In light of the urgent need to mitigate climate change and the wide interest in carbon dioxide (CO_2) sequestration and conversion, CO_2 electroreduction (CO_2R) has emerged as as an attractive prospect towards establishing a sustainable carbon cycle. When coupled to renewable electricity, CO_2R would allow for the storage of intermittent renewable resources at ambient pressures and temperatures, produce fuels and chemicals, all the while reducing CO_2 emissions.[1] Gold-based materials are the most active and selective catalysts for the production of CO, a critical component of syngas.[2] Understanding the reaction mechanism on Gold-based catalysts is therefore a critical step towards designing new catalyst materials, and is the focus of the present joint theoretical-experimental study.

While it is generally accepted that CO_2R to CO proceeds through *COOH and *CO intermediates, the rate-limiting step remains a topic of significant controversy. On the basis of recent Tafel analysis and kinetic isotope effect (KIE) studies, three different reaction steps have been postulated to be rate-limiting: electron transfer to CO_2 and concomitant adsorption,[3,4] proton transfer to *CO_2 to form *COOH or *COOH to form a protonated *COOH complex[5] or electron transfer to *COOH to form *CO.[6] In this work, we will discuss reasons for the controversy and present experimental and theoretical evidence for field-driven CO_2 adsorption as the limiting step.

Recently, a few attempts have been made to develop kinetic models for CO_2 reduction to CO based on *ab initio* reaction energetics, which focus primarily on Ag.[7,8] A previous study has also constructed a kinetic volcano for CO_2 reduction to CO based on an electrochemical barrier fitted from experiment along with *ab initio* calculations of reaction thermodynamics.[9] Due to the complexity of the reaction network, Rossmeisl *et al.* also correlated reaction thermodynamics directly with product selectivity in CO_2R in a phenomenological manner.[10,11] The theoretical studies suggest differente rate-limiting steps, which could arise from the vastly different methodologies and model assumptions, and highlights the need for a new, unified multi-scale modeling approach. In addition, recent studies have stressed the importance of mass transport phenomena.[12–15] Attempts have been made to include these in kinetic models,[8,12,16] however without considering the presence of the charged double layer. The significant impact of the electric double layer field on the energetics of critical reaction steps has also been sug-

[a)] Electronic mail: sringe@stanford.edu

[b)] Contributed equally to this work.

[c)] Electronic mail: kchan@fysik.dtu.dk

gested by recent studies.[7,17–20] Here, we show that the double layer plays a critical role for both kinetics and mass transport by controlling the pH and reactant concentrations at the reaction plane.

In what follows, we first present CO_2R experiments on Gold at acidic pH values similar to a recent study by Varela *et al.* on single-site catalysts.[21] Where hydronium cations are proton donors, the first CO_2 adsorption step and the proton-coupled electron transfer (PCET) steps can be clearly distinguished by their pH dependence. We can therefore attribute the invariance of the CO production rate to the CO_2 adsorption step being limiting. We develop a micro-kinetic model based on surface charge-dependent *ab initio* derived reaction energetics. The kinetics are coupled to a detailed continuum model that integrates, for the first time, the structure of the electric double layer, buffer equilibria, diffusion and migration. The simulations confirm the CO_2 adsorption step to be rate-limiting. We show the experimental Tafel slope to arise from the potential dependence of the surface charge density and corresponding electric double layer field, which drives the adsorption of CO_2. At very low overpotentials, the reaction rate is limited by the conversion of *COOH to *CO. We also find that the double layer charging reduces the local pH at the reaction plane making CO_2 adsorption a more likely rate-limiting step than the formation of *COOH. These results together demonstrate the critical role played by the structure of the electric double layer on both the rate of field-driven processes and the local pH, which drives proton transfers in almost all electrochemical energy conversion processes.

Results

Reaction mechanism. Figure 1 shows the commonly discussed reaction mechanism for CO_2R on Gold electrodes, applied in this work.[5,22,23] The process is initiated by the adsorption of CO_2. As CO_2 approaches the surface, it bends, resulting in a stabilization of the lowest unoccupied molecular orbital (LUMO) and a partially negative, bound $*CO_2$ intermediate[5,24] which can be stabilized by the interfacial electric field.[7,18–20] The CO_2 adsorption step is followed by two proton-coupled electron transfers (PCETs) to yield the *CO intermediate which readily desorbs due to the weak CO–Au binding energy.[25]

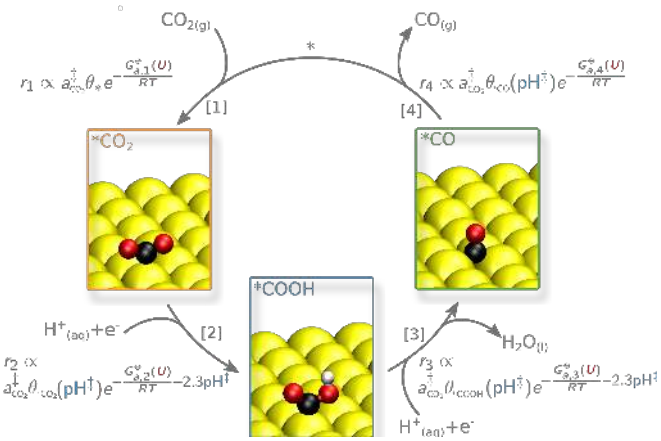

FIG. 1: Considered reaction mechanism for CO_2R on Gold. The gray equations depict the measurable CO production rate r_k in the case that the corresponding reaction step k is limiting the overall conversion process, $a_i^{\ddagger}$ and $pH^{\ddagger}$ depict species activities and pH at the reaction plane. All equations are given for acidic reaction conditions on an absolute potential reference scale. The coverage of empty sites (θ_*) is roughly pH-independent, since it is always close to one on Gold.

Experimental evidence for the rate-limiting step. While the mechanism illustrated in Figure 1 is generally accepted, the rate-limiting step remains controversial. In recent literature, proton transfer to $*CO_2$ or *COOH[5] as well as *COOH to *CO[6], but also CO_2 adsorption with concomitant partial electron transfer[3,4] has been discussed to be limiting.

To elucidate the rate-limiting step, we performed pH dependent CO_2R experiments over an acidic to neutral pH range. Considering first CO_2 adsorption to be limiting the CO production rate, the CO production rate would show no pH dependence on an absolute potential reference scale (e.g. on the Standard Hydrogen Electrode – SHE scale) following the rate expressions presented in Figure 1 (cf. also Supplementary Note 1). For this to be true, also the coverage of empty sites should be pH independent. On Gold, experiments and theoretical results as well as our simulations below suggest small coverages of reaction intermediates,[3,26,27] in which case the relative change of the coverage of free active sites with a change of the pH is negligibly small. In contrast to CO_2 adsorption, all other reaction steps depend on the pH via the coverages or the thermodynamic driving force, suggesting that the pH dependence can be used to distinguish the rate-limiting step.

Figure 2 shows the experimentally obtained partial current density for H_2 (upper panel) and CO (lower panel) production on an SHE scale under the influence of different pH values and buffering conditions (faradaic efficiencies are presented in Supplementary Note 2, in particular Supplementary Figures 1-4 and Supplementary Tables 1-4). Firstly, a clear shift of the curves with pH is observed in the HER case. Due to the small concentration of protons at pH = 6.8, water would be the dominant proton donor. At pH = 3.0, the proton activity increases significantly and, with it, the HER overpotential drops. Due to the higher acidity of hydronium ions compared to water, they would dominate the proton-transfers to adsorbates. Figure 2 also shows the activity of an unbuffered solution. In the HER activity, there is a plateau in the intermediate potential region, which can be attributed to mass transport limitations of protons.[28] We additionally observed a decrease in the rate of HER in unbuffered systems as a result of an increase in pH over

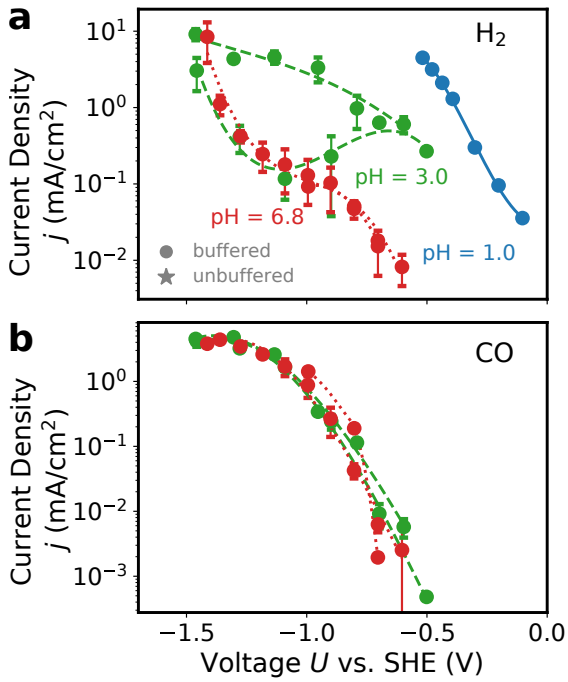

FIG. 2: Experimental CO_2R polarization curves. **a** H_2 **b** CO partial current density. The data was obtained from running CO_2R on poly-crystalline Gold at various bulk pH conditions. The filled circles refer to bicarbonate or phosphate buffered solutions held at fixed pH values of 7 and 3, respectively, and the stars refer to solutions using bicarbonate in a non-buffered regime. The vertical error bars represent the standard deviation resulting from three separate measurements.

the duration of the experiment and at more negative potentials. The slight increase in pH which we kept below 0.5 units (reported in the experimental section) will be proportional to the total number of charges passed during the experiment. From the Nernst equation, this increase would lead to an estimated decrease in HER rate by 68 % in agreement with our experiment. Going to more negative overpotentials, the strong faradaic currents reduce the proton activity at the electrode until water becomes a more facile proton donor and the current density approaches the one at pH = 6.8 conditions.[29]

CO production was observed under all pH conditions except at pH 1, where only H_2 could be collected. In contrast to the HER polarization curves, the CO partial current density is invariant with pH, as clearly seen from Figure 2. This invariance shows that the CO_2 adsorption step (independent of an additionally occurring electron transfer) is limiting the reaction rate, since otherwise the overpotential should also shift with pH, similar to the HER current densities. Also the observed lack of influence of the presence of buffer at pH 3.0 , could be seen as another hint for a non-proton transfer step to be limiting the reaction rate.

Kinetic Isotope Effect (KIE) experiments that compare activity in normal and deuterated water, in principle, may also allow one to differentiate between the chemical and PCET steps, since the former do not involve any proton donors. Reference[3] observed no discernable KIE and therefore postulated that CO_2 adsorption must be limiting the reaction rate. However, our calculations suggest that the conclusions from a KIE experiment are not necessarily unequivocal. As shown in the Supplementary Table 5 (Supplementary Note 3), we predict different KIEs based on changes of the zero point energy[30] for the $*CO_2$ to *COOH step and the *COOH to *CO step, with the latter being essentially negligible. Therefore, it would be possible that the rate-limiting step corresponds to the proton-electron transfer to *COOH to form *CO step, even when the KIE is negligible. In addition, the KIE effect can be convoluted with isotope effects related to mass transport, arising from differences in the diffusion constant of deuterated water or the acid dissociation constants, both of which would increase the local CO_2 concentration.[31]

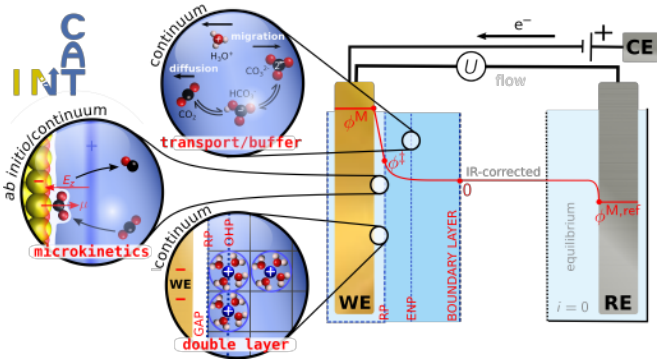

FIG. 3: Schematic illustration of the multi-scale approach to electrocatalytic CO_2 reduction. Reaction kinetics obtained from field-dependent DFT calculations are used to parametrize a micro-kinetic model. The model is coupled to a continuum mass transport model which models the diffusion, migration and reaction of species inside the boundary layer. This explicitly includes the double layer which electric field drives the reduction of CO_2 . The double layer model also includes the presence of a gap capacitance and cation repulsions at the outer Helmholtz plane (OHP) which are critical at the typically applied negative potentials. The thus defined multi-scale approach predicts the CO production rate as a function of applied electrode potential $\Delta\phi^{\mathrm{M}} = \phi^{\mathrm{M}} - \phi^{\mathrm{M,ref}}$ corrected for the IR potential drop. WE = working electrode, RE = reference electrode, CE = counter electrode, RP = Reaction Plane, ENP = Electro-neutrality Plane.

Multi-scale modeling. Figure 3 illustrates our integrated, multi-scale approach to model electrocatalytic CO_2 reduction. At the *ab initio* scale, we determine surface-charge density σ dependent reaction thermodynamics from density functional theory (DFT) calcula-

tions using a continuum solvent and planar counter charge representation on various facets of Gold (cf. Supplementary Note 4, Figures 7-10 and Table 6 for all results). The dependence of all thermodynamic states on the applied cell voltage U is expressed via the Computational Hydrogen Electrode approach (CHE).[32] More details can be found in the Methods section and the Supplementary Note 1. The resultant voltage- and surface charge-dependent mean field microkinetics are coupled to a Poisson-Nernst-Planck mass transport model integrating a continuum representation of the double layer structure, the effect of cation-cation repulsion and associated finite ion size effects, diffusion, migration, and buffer equilibria within the boundary layer of the working electrode. In contrast to previous electrochemical mass transport models,[8,12,16] our scheme accounts for the electrostatic interaction of charged species with the charged electrode, which we show to be critical to rationalizing the CO_2R activity. We further use Robin boundary conditions to relate the surface charge density parameter in the DFT calculations to the applied cell voltage $\sigma(U)$. The self-consistent solution of steady-state kinetic rate and stationary mass transport equations has been implemented into our newly developed *Cat*alysis at the *I*nterfacial *N*ode to *T*ransport phenomena (`CatINT`) program package, which is described in detail in the Methods part of manuscript and Supplementary Information (cf. in particular Supplementary Figure 23 for a schematic representation).

Computational evidence for the rate-limiting step. Figure 4 shows the dependence of the formation energy of all reaction intermediates on the surface charge density. *CO_2 showed a significant dependence on the interfacial field while all other states were relatively independent. Recent studies on the CO_2 adsorption process showed that the transition state is structurally very close to the *CO_2 state.[24] Analogously, we found the *CO_2 to *COOH transition state to be close to *COOH by performing NEB-DFT calculations and extrapolating to a constant potential[33] (cf. Supplementary Figure 5). In case of the *CO_2 state being less stable than the *COOH step, also a concerted mechanism from $CO_{2(g)}$ to *COOH could be imagined. Using NEB calculations, we found this pathway, however, to be kinetically hindered (cf. Supplementary Figure 6). These results suggest that the reaction thermodynamics of *CO_2 and *COOH describe the kinetics of the first two step reasonably well. The *COOH to *CO step, in contrast, exhibits a potential-dependent kinetic barrier. Due to methodological problems to evaluate this barrier accurately, we left as a variable parameter and later discuss its influence on the obtained results in the paragraph "CO_2 adsorption". The symmetry factor β for this particular step is chosen as 0.5.

Recent experiments have indicated that CO_2R on poly-crystalline Gold happens predominantly at under-coordinated surface sites.[19,34] Following this, we considered a stepped (211) facet as active site and refer the interested reader to the Supplementary Note 5 for a more detailed discussion on the facet dependence. The (211) facet was chosen as a proto-typical under-coordinated site based on previous theoretical data that suggested the *COOH binding energy to be relatively invariant with the step site model.[19] From Figure 4 we find *CO_2 to be strongly stabilized by increasing negative surface charge and the corresponding interfacial electric field, while *COOH and *CO are less substantially effected.

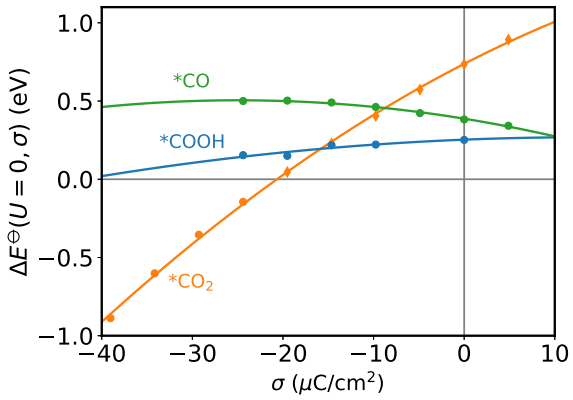

FIG. 4: Surface charge dependent formation energies. The formation energies $\Delta E^{\ominus}$ are given for the key reaction intermediates *CO_2 , *COOH and *CO. Energies are referenced to CO_2 and H_2O in the gas phase, without correction for zero point energy or finite temperature. The dependence on surface charge density σ at the (211) facet of Gold is shown without regard of the CHE-Frumkin potential-dependent term in Eq. 5. In the case of *CO_2 , the formation energy for surface charge densities > -20 μC/cm^2 was obtained from single point calculations using a constrained *CO_2 geometry.

Using the surface charge dependent intermediate formation energies, we set up a mean-field micro-kinetic model for the elementary reaction steps given in Figure 1. We adopted the pH = 6.8 experimental conditions that were presented in Figure 2 and assumed water as a proton donor for the electrode reactions. Due to the neutral pH, we considered the presence of both proton- and hydroxide driven buffer reactions, in contrast to previously published multi-scale modeling of CO_2R .[8,12] HER was not included in the multi-scale modeling approach for several reasons. First of all, previous theoretical studies found small binding energies of all reaction intermediates[26] suggesting negligibly small coverages. Experiments based on ATR-SEIRAS spectroscopy[3,27] have additionally not observed any higher coverages of species. These theoretical and experimental findings suggest that there is effectively no competition for active sites. HER could be also thought as changing the local pH and thus effecting CO production. We found, however, that HER partial current density is lower than the CO current by orders of magnitude at pH = 6.8 in all but the highly

mass transport limited regions (< 1.5 V vs. SHE) (cf. Supplementary Figure 4). From this, we conclude that HER likely cannot change the pH enough to alter the CO current. This is supported by the fact that the CO evolution rate remains constant at low overpotentials in both pH 6.8 and 3.0, even though the HER rate is almost 100 times higher in pH 3.0 (cf. Figure 2).

The mapping of the turn over frequency (TOF) obtained from the micro-kinetic modeling to a current density, requires an estimate for the active site density. Recent experimental studies correlated the CO production activity with the density of grain boundaries on Gold surfaces.[35] The reported grain boundary density of $2.873\,\mu\mathrm{m}^{-}1$ for poly-crystalline Gold corresponds to an active site density of $\rho_{\mathrm{act}} = 9.6{\cdot}10^{-5}$ sites/Å^2 considering (211)-like atomic distances. Using this value, we achieved a nearly quantitative prediction of the CO partial current density. We stress that a realistic value for the active site density is essential, since the absolute current density determines the mutual dependence of mass transport and kinetics which depends sensitively on the absolute current. All other parameters for the multi-scale model are documented in Supplementary Table 7 (Supplementary Methods).

Figure 5 shows the CO partial current density curves as obtained from coupled micro-kinetic-transport modeling using `CatINT` (cf. Supplementary Note 7 for further results which are discussed in detail below). The curvature and slope of the curve show good agreement with the present experimental data and also with previous studies from Hori *et al.*,[36] Dunwell *et al.*[5], Chen *et al.*[37] and Wuttig *et al.*.[3] We performed a degree of rate control (DRC) analysis on our data, where the DRC is defined as the change of the CO production rate with the free energy of a particular state assuming constant activities of all species:[38]

$$\mathrm{DRC}_m = \frac{d\log(r_{\mathrm{CO}})}{-d(\tilde{\mu}_m/RT)} \quad . \tag{1}$$

$\tilde{\mu}_m$ represents either of the electrochemical potentials of *CO_2 , *COOH or *CO or the *COOH to *CO transition state ("*CO-OH$^{\mathrm{TS}}$") energy. From the DRC analysis, we found the *COOH to *CO transition state to exhibit the strongest influence on the CO production rate and thus to be rate-limiting in the low overpotential region. In the intermediate and high overpotential region, we found *CO_2 adsorption to be rate-limiting instead.

In the low overpotential region, we found a small Tafel slope of 42 mV/dec, close to experimental measurements on oxygen-derived (OD) Gold (cf. Figure 5). OD-Gold electrodes, due the their high roughness factors, enable us to probe this region. Since the *COOH to *CO step is limiting the reaction rate, the overpotential depends on the kinetic barrier of the *COOH to *CO step. At higher overpotentials (< -0.7 V vs. SHE), the DRC suggests that *CO_2 adsorption controls the conversion to CO. The determined Tafel slope of 101 mV/dec for CO production is in the range of experimentally reported values (cf. Figure 5). This also suggests that *COOH to *CO cannot be limiting the reaction rate at these electrode potentials, because this would require a symmetry factor deviating significantly from the commonly considered 0.5[5] in order to reproduce the same slope. Furthermore, the kinetic barrier for the *COOH to *CO step would need to be considerably larger than the chosen value of 0.6 eV at 0 V vs. SHE. For comparison, potential-extrapolated NEB calculations using DFT found a kinetic *COOH to *CO barrier of only 0.66 eV on Pt(111).[39] We thus conclude that *COOH to *CO is unlikely to limit to the activity in higher overpotential regions.

Finally, we also comment on the simulated *CO coverage. As shown in Figure 5, the *CO coverage is essentially zero over the whole potential range. Previous studies found a 20 % *CO coverage at all potentials $<$ -0.8 V vs. SHE using ATR-SEIRAS spectroscopy,[3] which was, however, later suggested by ref.[6] to arise from Pt

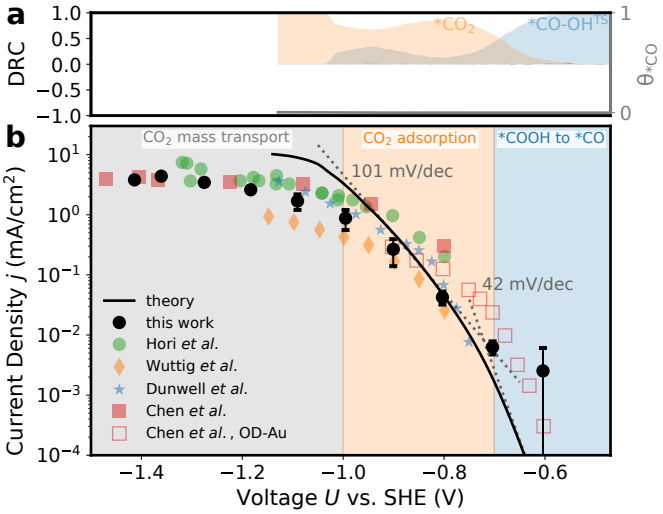

FIG. 5: Multi-scale CO_2 reduction simulation results compared to experiment. **a** Simulated degree of rate control (DRC), where a positive (negative) value indicates that the considered reaction intermediate needs to be stabilized (destabilized) in order to enhance the rate and boundary values of 1 and -1 represent full rate control by the intermediate. *CO-OH refers to the *COOH to *CO transition state. The *CO coverage is shown as a gray line (plotted with respect to the right axis). **b** CO polarization curve, where the solid line shows the multi-scale simulation result compared to experimental results from this work (0.1 M $KHCO_3$, pH = 6.8, black filled circles) and previous studies using 0.5 M $KHCO_3$ (pH = 7.2) of Dunwell *et al.*,[6] Wuttig *et al.*[3], Hori *et al.*[36] and Chen *et al.*[37](filled colored symbols). Data has been generally obtained using poly-crystalline Gold electrodes, despite the additionally shown data from ref.[37] on oxygen-derived nano-porous Gold electrodes (normalized using a roughness factor of 72). Tafel slopes from our model are indicated as dotted lines.

impurities. The latter authors could not detect any *CO coverage under reducing conditions all the way down to -1.0 V vs. SHE, which is also in line with later studies that measured down to -0.9 V vs. SHE.[27] These results together with ours thus suggest that *CO coverage is indeed negligible under CO_2R conditions.

Carbon dioxide adsorption. Considering CO_2 adsorption as the rate-limiting step, there are two major contributions to the apparent Tafel slope, A_{Tafel}: the charging properties of the surface and resulting stabilization of the $*CO_2$ state, as well as $*CO_2$ mass transport contributions. Considering that the coverages of all species are negligibly small, the Tafel slope can be expressed as follows (cf. Supplementary Note 6 for the derivation):

$$A_{\mathrm{Tafel},1} = \left| -\log_{10}(e)\frac{\Delta a_{\sigma,1} + 2\Delta b_{\sigma,1}\sigma}{RT}\underbrace{\frac{\partial\sigma}{\partial U}}_{C_{\mathrm{dl}}} + \frac{d\log(a^{\ddagger}_{\mathrm{CO_2}})}{dU}\right|^{-1}, \tag{2}$$

where $a^{\ddagger}_{\mathrm{CO_2}}$ is the activity of CO_2 at the reaction plane. In the first part, $\Delta a_{\sigma,1}$ and $\Delta b_{\sigma,1}$ depict the linear and quadratic surface charge dependence of the $*CO_2$ formation energy (cf. Eq. 5 in the Methods part), where in this case $\Delta b_{\sigma,1}$ is relatively small. C_{dl} represents the double layer capacitance which is roughly constant with applied voltage (cf. Supplementary Figure 12). This results in the linear dependence of the $*CO_2$ formation energy on the surface charge density in Figure 4 and eventually to a nearly constant Tafel slope in the kinetic region (cf. Figure 5). The reader is referred to the Supplementary Note 6 for an analogous expressions for the PCET steps.

As seen from Figure 5, this strategy leads to a Tafel slope of 101 mV/dec for the CO_2 adsorption step which agrees reasonably well with the experimentally reported range of values 120–150 mV/dec in the intermediate potential range. This good agreement with the experimental data can be seen as support of our reaction mechanism that considers field driven CO_2 adsorption as the first reaction step, followed by two PCETs. Previous Tafel analysis assumed a full electron transfer to CO_2 and a symmetry factor of 0.5, which results in a Tafel slope of 120 mV/dec. It the present work, we explicitly simulate the partial transfer of charge that occurs with CO_2 adsorption, and the resultant dipole that interacts strongly with the interfacial field. The potential dependence of the interfacial field gives rise to the potential dependence of CO_2 adsorption.

We also performed experiments to evaluate the sensitivity of CO and H_2 production towards exchange of the electrolyte-containing cations (cf. Supplementary Note 8, Figure 22). From this, we found a strong cation effect on the CO production rate, while the HER rate was nearly unchanged. This is in line with our recent work,[20] that showed that smaller hydrated cations as Cs^+ are highly concentrated in the Helmholtz layer giving rise to an increased interfacial electric field. This makes cation exchange a way to probe the field-sensitivity of the rate-limiting step, and in accordance with our results above, we find the CO production rate to be highly sensitive, in contrast to the HER rate. Interestingly, we also find the Tafel slope to decrease in a relatively higher overpotential region for Cs^+ which could be due to a strong stabilization of $*CO_2$, making the *COOH to *CO step limiting until higher overpotentials.

Mass transport of carbon dioxide. The last term in Eq. 2 is defined by the mass transport of CO_2 to the electrode. Figure 6 shows the potential-dependent species activities at the reaction plane as obtained from our multi-scale model (cf. also Supplementary Figures 13 and 14 for position- and potential-dependent concentrations, respectively). We found the CO_2 activity to be constant in the low overpotential region and decrease due to CO_2 deficiency at the reaction plane at higher overpotentials. The decreased activity leads, according to Eq. 2, to an increase of the Tafel slope and the observed leveling off in the experimental and theoretical polarization curves (cf. Figure 5). By increasing the boundary layer thickness, we found a decrease of the CO production current at high overpotentials, which confirms the limitation by CO_2 mass transport (cf. Supplementary Figure 15).

The double layer has two main effects on the mass transport. First, it leads to migration of positively charged species as K^+ or H^+ towards the negatively charged electrode, and repels anions (cf. Supplementary Figure 16). Secondly, under the high applied overpotential and the positive PZC of Gold, the potassium concentration at the OHP is nearly fully saturated (cf. Supplementary Figures 13 and 14). In the GMPB model, this induces repulsive interactions which limit the K^+ concentration and make it roughly constant over the considered voltage range. Besides K^+, other species concentrations are also affected by the repulsive interactions, changing e.g. the local pH or the water dissociation equilibrium (cf. Supplementary Figures 13, 14, 17 to 19). In particular, the local CO_2 concentration at the reaction plane is reduced relative to the ENP as shown in Figure 6 **b**. We also tested the inclusion of a finite size of $a_i^{\mathrm{cell}} = 4$ Å for all other species than potassium. Due to the much smaller concentration, we found this, however, to not have any effect on the activity coefficient (Eq. 9) and also not on the CO production rate. The local depletion of species is thus only a function of the effective K^+ size used in the model. The catalytic conversion rate, however, depends only on the species' activities, which are not affected by the repulsive interactions, due to the cancellation of the activity coefficient increase and the concentration decrease.

Voltage dependent species distribution. Recently, CO_2 concentration profiles were measured at a

bulk pH of 7.3 using ATR-SEIRAS spectroscopy which effectively probes a region of around 5–10 nm distance to the electrode.[14]. Figure 6 **b** compares these experimental values with the calculated potential-dependent local CO_2 concentration at 10 nm from the reaction plane. In the following, we will refer to this distance as the electroneutrality plane (ENP, cf. Figure 3), since the double layer extends to about this distance. Theoretical values at the ENP appear to be consistent with the experimental values under non-stirred experimental reaction conditions. The comparison also shows, that although the CO_2 concentration at the reaction plane is affected by repulsive interactions, the CO_2 activity is not. The CO_2 activity is thus not subject to double layer charging effects and is the same at both reaction plane and ENP.

Figure 7 **a** shows the potential dependence of the local pH at the ENP compared to ATR-SEIRAS spectroscopy[14]. In agreement with the experimental data, we find the pH to behave bulk-like at lower overpotentials and increase due to the higher CO production rate and consumption of protons at higher overpotentials.[12,14] The non-zero species fluxes at the electrode perturb the double layer and lead to concentration profiles deviating significantly from equilibrium Poisson-Boltzmann theory (cf. Supplementary Figure 20). At high overpotentials, both theory and experiments predict inverse trends, with lower bulk pH values resulting in in a higher local pH at the ENP. We explain this by the increased bicarbonate buffer concentration in the higher bulk pH solutions, e.g. in the case of pH 7.55 (0.53 M $KHCO_3$) compared to pH 7.0 (0.15 M $KHCO_3$). This ensures a better buffering of the produced hydroxide anions at the electrode keeping the pH closer to the bulk pH. We note that the fact that we overestimate the pH in the high overpotential region could be attributed to differences in the cell hydrodynamics, where our model predicts a smaller pH with increased boundary layer thickness (inverse trend to what was observed before[12]). Also the HER, not considered in the theoretical model, could be sensitive to the bicarbonate concentration[29], which would lead to local pH changes.

At the reaction plane, the generally negative surface charge at the electrode leads to an increase in the local concentrations of cations and a decrease in those of anions. The primary effect of this electrostatic interaction is the increased concentration of protons and the resultant stabilization of the *COOH state relative to the $*CO_2$ state by 120–240 meV (cf. Figure 1). In consequence, $*CO_2$ adsorption becomes a more likely rate-limiting step in the production of CO. This result points to the importance of the double layer structure on resultant activity, hitherto neglected in previous work.

Bicarbonate reaction order. Since with CO_2 adsorption a pH-independent process is determining the reaction rate, the CO production rate depends only on the local concentration of CO_2 at the reaction plane. Recent studies further investigated the influence of bicarbonate on the CO production rate (bicarbonate reaction order) and obtained varying answers.[3,6] The determination of the bicarbonate reaction order is complicated by the strong dependence on the local pH, diffusion and migration effects as the coupling to the local CO_2 concentration. By varying the bicarbonate concentration, keeping the total ionic strength constant and normalizing the current density using the local CO_2 concentration, Dunwell *et al.* found a 0.9 reaction order indicating the role of bicarbonate in transporting the reactive CO_2 species to the electrode.[6] Within our modeling approach, we test this finding directly by considering two separate CO_2 species, one reacting at the electrode, and the other participating in the buffer equilibria. By this we found that no change in the CO production rate compared to our above discussed simulations, indicating that the buffer equilibrium does not produce reactive CO_2 . This is also indicated by the buffer CO_2 activity being only slightly reduced at high overpotentials (cf. Supplementary Figure 21).

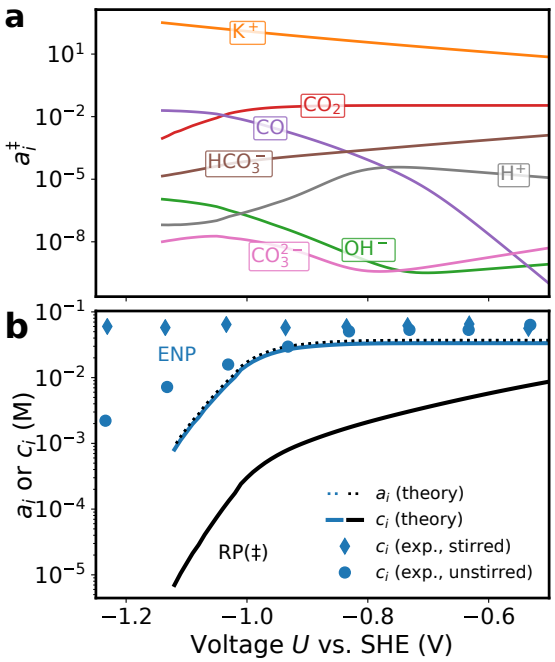

FIG. 6: Voltage dependence of activities at the reaction plane. **a** Species activities at the reaction plane (RP, ‡) as a function of electrode potential $\Delta\phi^{\mathrm{M}}$ as predicted by the coupled micro-kinetic-mass transport modeling scheme using `CatINT` (bulk pH of 6.8). **b** CO_2 concentration and activity at the reaction plane (RP, ‡) and electro-neutrality plane (ENP, 10 nm distance from RP) compared to the ATR-SEIRAS spectroscopic results from ref.[14], all evaluated at a bulk pH of 7.3. The dots and diamonds denote non-stirred and stirred reaction conditions in the experiments, respectively.

Discussion

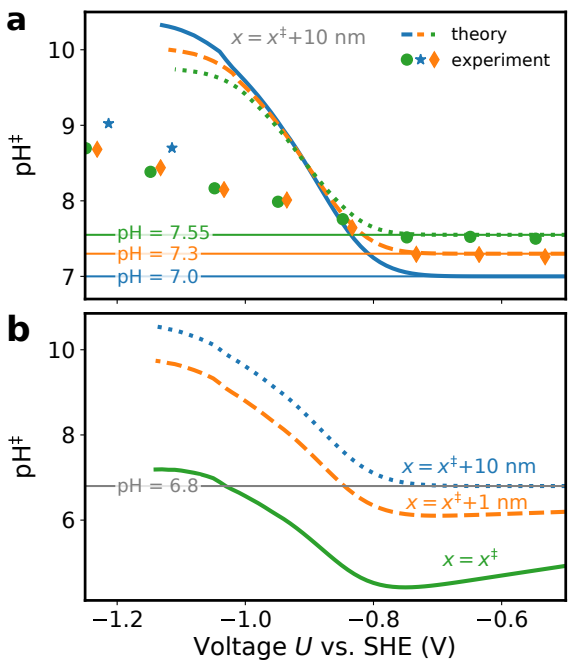

FIG. 7: Voltage dependence of the local pH. **a** Local pH at the ENP (10 nm) as a function of electrode potential as predicted by the coupled micro-kinetic-mass transport modeling scheme using `CatINT` (solid lines) and ATR-SEIRAS spectroscopy (symbols) of ref.[14] for three different bulk pH values. **b** Modeled local pH at three different distances from the electrode, the reaction plane (RP, ‡), 1 nm distance and 10 nm distance (electro-neutrality plane, ENP). The horizontal line indicates the bulk pH of the simulations and experiments.

Gold remains among the most active and selective CO_2R to CO electrocatalysts to date, and elucidating the mechanism for this process is therefore of critical importance to the development of improved CO_2R catalysts. In performing new CO_2R experiments at acidic pH values, we find the H_2 partial current density to substantially shift with pH on an absolute SHE potential scale, indicating a proton-electron transfer to be limiting the conversion rate. In contrast, we find that the CO production rate is insensitive to the bulk pH, which suggests that the first reaction step not involving the transfer of a proton is limiting the conversion rate.

In order to derive a more thorough understanding of the involved processes, we developed a new multi-scale approach, coupling micro-kinetics with a detailed account of mass transport phenomena such as diffusion, migration and buffer reactions. In contrast to previous approaches, we explicitly integrated the structure of the electric double layer which we found to be critical to determining the electrocatalytic activity.

By applying this model, we obtained excellent agreement with the major features of the experimental polarization curve and qualitative agreement with ATR-SEIRAS spectroscopic measurements of previous studies[14]. In detail, we rationalized the previously reported Tafel slope of around 40–60 mV/dec at very low overpotentials by a rate-limiting *COOH to *CO step and the Tafel slope of around 120–150 mV/dec at most of the relevant potential window by a rate-limiting CO_2 adsorption step and thereby resolved a long-standing controversy in the literature.[3,5,6] We found the measured Tafel slope for CO_2 adsorption to arise from the potential dependence of the surface charge density which stabilizes the dipolar $*CO_2$ state that is created due to partial electron transfer and molecule bending. The origin for the kinetic limitations is therefore not an electron transfer, but the field-dependent stabilization of the $*CO_2$ state. At high overpotential, the CO current is limited by CO_2 diffusion limitations. Besides that, we also show that the negative charge of the electrode critically reduces the local pH at the reaction plane. Finally, our model shows that all reactive CO_2 diffuses to the electrode from the boundary layer and bicarbonate buffer does not significantly increase the amount of reactive CO_2 under stationary reaction conditions.

These new findings from experiments and multi-scale modeling highlight the role of surface charging in electrocatalysis and open possibilities for improving catalyst conversion efficiencies and product selectivities. In particular, non-PCET reaction steps that involve the transfer of partial electrons and the creation of a strong dipole moment as discussed here have been found to limit important electrochemical processes as the formation of C_2 products on Cu.[17,18,20] Our results suggest that such processes can be generally activated by improving the charging properties of the solid-liquid interface, by changing the potential of zero charge, e.g. via co-adsorbates or introducing impurities into the Gold electrode, by varying the Helmholtz gap capacitance, by changing the size or charge of the electrolyte containing cations,[20] or by applying an external field via a field-effect transistor.[40] Further, the here discovered sensitivity of the reactive pH on the charge of the electrode could be important to tune the product selectivity or activity of pH-sensitive reactions.[41] The new insights and identified descriptors therefore constitute an important piece towards the strategic optimization of electrochemical processes.

Methods

Experimental. The electrochemical testing setup used for CO_2R on gold foil electrodes has been extensively described in the literature.[42,43] In brief, the custom-built electrochemical cell consists of two cell compartments partially filled with electrolyte and separated by an ion conductive membrane. This electrochemical cell, characterized by a high ratio of electrode area (5.8 cm^2) to electrolyte volume (10 mL), was used to conduct short duration potentiostatic experiments using freshly cleaned Gold and Platinum foils as the respective working and counter electrodes. Before each experiment, the Gold foil (thickness 0.1 mm, Alfa Aesar, 99.9975+% metal basis) was submerged in a 40 vol% aqueous nitric acid solution (Fisher Scientific, Certified ACS Plus) for at least 15 minutes to remove metal contaminants. The Gold foil was then rinsed with

Millipore water and dried with a nitrogen flow before the assembly of the electrochemical cell. A similar pretreatment was carried out for the platinum foil used as counter electrode. Three types of ion-exchange membranes were used in this work depending on the pH and nature of the electrolyte tested. These were anion-exchange membrane for experiments near neutral pH (Selemion AMV; AGC), bi-polar membranes (Fumasep FBM, FuMA-Tech GmbH, Germany) for experiments at pH 3.0 and proton-exchange membranes (Nafion 117, Fuel Cell Store Inc., USA) for experiments at pH 1.0. CO_2 gas (5.0, Praxair) was constantly bubbled at a rate of 20 sccm through both electrolyte compartments using a glass gas dispersion frit previously described.[44]

Two types of electrolytes were used for the CO_2R experiments, namely, buffered and unbuffered electrolytes. Buffered electrolytes such as bicarbonates and di-hydrogen phosphates maintain a constant bulk pH in both cell compartments throughout the length of the experiment independently of the ion membrane and pH used. On the other hand, electrochemical testing in unbuffered electrodes leads to the increase of pH in the working electrode which is exacerbated at higher current densities. In order to alleviate the pH change with the progress of the experiment, a bi-polar membrane was used to split water and generate protons and hydroxyl ions to respond to pH changes. However, it must be noted that bipolar membranes did not completely suppress pH variations for experiments carried out at pH 3.0 in the unbuffered $KClO_4$ electrolyte and for these reasons potentiostatic experiments were limited to only 4 minutes in duration. These short experiments are enough to obtain a complete product quantification while limiting pH variations to below 0.5 units of pH even in high current experiments. Experiments at pH 1.0 used a cation-exchange membrane and did not result in any measurable pH variations. High purity $KHCO_3$ (Sigma Aldrich; 99.99% trace metals basis), $KClO_4$ (Sigma Aldrich; 99.99% trace metals basis), KH_2PO_4 (Sigma Aldrich; purity ⩾99.0%), perchloric acid (70% $HClO_4$, Suprapur, Merck), CsOH (Sigma Aldrich; 99.95% trace metals basis) and $NaHCO_3$ (Sigma Aldrich; ⩾99.7% ACS reagent) were obtained from commercial sources and used without any further purification to prepare the electrolyte solutions. All aqueous electrolytes were prepared using high purity Millipore water. Gas products were detected using an on-line gas chromatography. The boundary layer thickness in this electrochemical cell has been determined to be $80\,\mu$m, using the diffusion limited current for ferricyanide reduction.[45]

Voltage- and surface charge-dependent kinetics. Figure 1 illustrates the CO production rate expressions resulting from the different steps being limiting. The expressions are written as a function of the applied electrode potential U:

$$U = \Delta\phi^{\mathrm{M}} + \Delta\mu^{\mathrm{M}} \quad . \tag{3}$$

Here, $\Delta\phi^{\mathrm{M}} = \phi^{\mathrm{M}} - \phi^{\mathrm{M,ref}}$ refers to the working electrode electrostatic potential relative to the reference electrode (here the Standard Hydrogen Electrode – SHE) and $\Delta\mu^{\mathrm{M}}$ is the chemical potential difference of both electrodes. The driving force for any coupled proton-electron transfer referenced to SHE is given by

$$U_{\mathrm{F}} = U + (2.3RT\mathrm{pH}^{\ddagger}/F - \phi^{\ddagger}) \quad . \tag{4}$$

Here, $\mathrm{pH}^{\ddagger}$ refers to the pH, and $\phi^{\ddagger}$ to the electrostatic potential at the reaction plane (RP, ‡). The additional terms that correct U are generally referred to as Frumkin[46] corrections. They arise from the potential drop in the diffuse layer of the working electrode. We note that the IR potential drop is usually corrected out in experiments and thus ignored here. All potentials are shown in Figure 3 and are given relative to the bulk electrolyte.

Considering this corrected driving force, we set-up a thermodynamic model to describe electrochemical reaction steps based on the Frumkin-corrected[46] Computational Hydrogen Electrode (CHE).[32] For a transfer of n proton-electron pairs, the free reaction energy change from initial to final state becomes

$$\Delta G_m(U) = \Delta G_m(U(\sigma=0)) + \underbrace{nF\left(U-\phi^{\ddagger}\right)}_{\text{full CT/CHE-Frumkin}} + \underbrace{\Delta a_{\sigma,m}\sigma(U) + \Delta b_{\sigma,m}\sigma^2(U)}_{\text{partial CT/field-dependence}} \quad , \tag{5}$$

where m refers to the index of the reaction step, F the Faraday constant, σ the surface charge density. $a/b_{\sigma,m}$ are parameters representing the surface charge dependence of a particular state and $\Delta G^{\circ}_m(U(\sigma=0))$ is the reaction energy at 0 V vs. SHE. The CHE model considers the potential dependence that evolves from the transfer of an integer numbers of electrons and protons between counter and working electrode via a coupled process.[47] This expression is extended by the sensitivity of the intermediate reaction states towards non-vanishing surface charge density at a particular applied electrode potential (cf. Supplementary Information for a detailed explanation and rationalization of our approach).

Implicit solvation schemes have become extremely popular in particular in electrochemistry,[20,48–53] due to their efficiency in treating solvation effects, but also the ability to incorporate simplified representations of counter charges. Here, we obtain the dependence of the reaction states on σ by fitting σ-dependent implicit solvent DFT calculations using a planar counter charge representation via the Environ module[54] of the DFT program package QUANTUM ESPRESSO.[55] The dependence on the surface charge is considered up to second order. Potential-dependent creation of surface charge $\sigma(\Delta\phi^{\mathrm{M}})$ can be obtained by integrating experimental double layer capacitance measurements as a function of electrode potential.[56] Alternatively, continuum theories can be utilized to provide an estimate of the double layer capacitance contribution, such as described in the next section. We recently showed that surface charge-dependent reaction energetics effectively captures the physics at the electrified solid-liquid interface, and enables us to elucidate the effect of cations on the electrochemical CO_2 reduction rate.[20]

We apply the Butler-Volmer approximation and consider a linear dependence on the potential (cf. Supplementary Information):

$$G^{\ominus}_{\mathrm{a,m}}(U) = G^{\circ}_{\mathrm{a}}(U(\sigma=0)) + \underbrace{\beta FU}_{\substack{\text{partial CT}\\ \text{(Butler-Volmer-Frumkin}\\ \text{+field-dependence)}}} \quad . \tag{6}$$

where β is the symmetry factor. β depends on the amount of charge transferred to the transition state, the charge-symmetry of the transition state, and the field-dependence of the activation energy. Higher order terms are ignored for simplicity.

Mass transport and double layer charging. We consider mass transport of CO_2, CO, protons, hydroxide anions as well as the buffer components K^+, HCO_3^- and CO_3^{2-} within a stationary, $80\,\mu$m thick boundary layer (cf Fig. 3). The transport of species in the electrolyte is modeled by the Nernst-Planck (NP) equation, in a generalized stationary form as:

$$\begin{aligned} \nabla\cdot j_i &= R_i \\ j_i &= -\frac{D_i}{RT}c_i\nabla\tilde{\mu}_i \\ \tilde{\mu}_i &= \mu_i^{\circ} + RT\ln(\underbrace{\gamma_i c_i}_{a_i}) + z_i F\phi \quad , \end{aligned} \tag{7}$$

with the species concentrations c_i, activities $a_i = \gamma_i c_i$, activity coefficients γ_i, fluxes j_i, diffusion constants D_i, the ideal gas constant R, the electrochemical potentials $\tilde{\mu}_i$, the species concentrations in the bulk solvent (outside the boundary layer) c_i°, the charges z_i and the electrostatic potential ϕ. R_i in Eq. 7 denotes a different source for the species i as for example buffer reactions which we include as kinetic rate expressions in the line of ref.[12] (cf. also Supplementary Information for all reaction equations). Coupled with the Poisson

equation

$$\varepsilon_{\mathrm{b}} \frac{d^2\phi}{dx^2} = -F \sum_i^N z_i c_i[\phi] = -\rho[\phi] \quad , \tag{8}$$

with the bulk dielectric permittivity ε_{b} and charge density ρ, we have the well-known Poisson-Nernst-Planck (PNP) equations. Under typical experimental reaction conditions, a constant flow of reactants is provided, so we therefore assume constant concentrations at the end of the boundary layer (cf. Figure 3).

We note that in the present work, in contrast to previous models, we consider explicitly the structure of the double layer. The resultant equation system is challenging in that it is highly nonlinear and includes variations within two vastly different length scales. For this reason, the electric double layer structure is mostly neglected in previous models through assuming global electroneutrality.[8,16,57,58] As further discussed below, however, even in the presence of a concentrated supporting electrolyte, the double layer does play a major role in both driving field-dependent electrochemical processes and in controlling the concentrations of charged species such as bicarbonate or protons at the reaction plane.

We also note that the activity coefficients γ_i are generally not 1 at the reaction plane. Considering the positive PZC of Gold at 0.16 V vs. SHE,[59] the surface is expected to be highly negatively charged under CO_2R conditions (−0.9 V vs. SHE), which leads to high supporting electrolyte cation concentrations. As a result, highly concentrated cations induce repulsive interactions with all species, which reduces their respective local concentrations. In the present work, we take the approach of the size-modified Poisson-Boltzmann model (MPB) (cf. Figure 3 a).[60] Essentially, the MPB model introduces a statistical lattice model in which each cell is only allowed to be occupied by a single species. The model can be generalized by assigning different lattice cell sizes a_i^{cell} to each species, which leads to the activity coefficients:[61]

$$\gamma_i = \frac{1}{1 - N_{\mathrm{A}} \sum_i^N c_i {a_i^{\mathrm{cell}}}^3} \quad . \tag{9}$$

The activity coefficients of all species are therefore reduced if the size of a particular species is increased. For species with small concentrations, the contribution to the activity coefficient is small. For this reason, we considered a non-zero size a_i^{cell} only for the highly concentrated and also due to their hydration shell large potassium cations, while the size of all other much less concentrated species were set to zero. The validity of this assumption is further discussed in the results. The K^+ cation diameter was chosen to be $a_{\mathrm{K^+}}^{\mathrm{cell}} = 8.2\,\text{Å}$ based on the K^+–Ag(111) distance obtained from X-ray diffraction studies.[62] The whole set of Eqs. 7 – 9 defines the Generalized Modified PNP (GMPNP) mass transport model used in this study.

The one-dimensional GMPNP equation is solved using the boundary conditions summarized in Table 1. Micro-kinetics and mass transport are coupled via a flux boundary condition at the reaction plane. The solution ϕ of the Poisson equation Eq. 8 The potential in the bulk solvent ϕ^{b} is set to zero by applying Dirichlet boundary condition The potential at the reaction plane $\phi^{\ddagger}$ is coupled to its gradient (proportional to the surface charge density) through a Robin boundary condition at the reaction plane (cf. ref.[63] and Supplementary Information):

$$\sigma = -\varepsilon_{\mathrm{b}} \left.\frac{d\phi}{dx}\right|_{x^{\ddagger}} = C_{\mathrm{gap}} \left[U - U^{\mathrm{PZC}} - \phi^{\ddagger}\right] \quad , \tag{10}$$

where U^{PZC} is the PZC of the working electrode relative to the reference electrode. Note, that the surface charge does not depend on the potential reference electrode, but only on the potential drop between reaction plane and metal relative to the PZC. The gap capacitance C_{gap} arises from quantum Pauli repulsion effects at the surface-water interface, which constitutes a significant part of the Helmholtz capacitance[64,65]. The constants defining the additional potential drop over the Helmholtz gap are the measurable cell potential U and the PZC, both given relative to an absolute reference potential (here SHE). We consider value of $C_{\mathrm{gap}} = 20\,\mu\mathrm{C/cm^2}$ for the gap capacitance according to the experimentally measured double layer capacitance[66–68] over almost the whole considered potential range (cf. Supplementary Figure 12). All other parameters are explicitly given and explained in the Supplementary Information. We define $x = x^{\ddagger}$ as the reaction plane similar to previous theoretical studies which located it at the outer Helmholtz plane (OHP).[69–71] Importantly, both choices lead to reactants being embedded into the double layer and therefore their concentrations to be sensitive to electrode charging effects.

TABLE 1: Boundary conditions used for the solution of the GMPNP equations. j_i^{GMPNP} and j_i^{MK} denote the species fluxes in the GMPNP mass transport model and microkinetic model, respectively. GMPNP = Generalized Modified Poisson-Nernst-Planck, bl = boundary layer.

equation	boundary	boundary condition
NP	$x = x^{\ddagger}(=0)$	$j_i^{\mathrm{GMPNP}} = j_i^{\mathrm{MK}}$
NP	$x = x_{\mathrm{bl}}$	$c_i = c_i^0$
Poisson	$x = x^{\ddagger}(=0)$	Robin
Poisson	$x = x_{\mathrm{bl}}$	$\phi = 0$

Data availability

All raw data of the surface charge density dependent DFT calculations of all reaction intermediates as well as the experimental CO_2 reduction experiments is provided in the Supplementary Information. Other data is available on request from the authors.

Code availability

`CatINT` is available free-of-charge at `https://github.com/sringe/CatINT` under the GNU GENERAL PUBLIC LICENSE. A program package documentation is provided at `https://catint.readthedocs.io/en/latest`.

References

[1] Chu, S., Cui, Y. & Liu, N. The path towards sustainable energy. *Nat. Mater.* **16**, 16–22 (2016).

[2] Wang, Y., Liu, J., Wang, Y., Al-Enizi, A. M. & Zheng, G. Tuning of CO2 reduction selectivity on metal electrocatalysts. *Small* **13** (2017).

[3] Wuttig, A., Yaguchi, M., Motobayashi, K., Osawa, M. & Surendranath, Y. Inhibited proton transfer enhances au-catalyzed CO2-to-fuels selectivity. *Proc. Natl. Acad. Sci. U. S. A.* **113**, E4585–93 (2016).

[4] Zhang, B. A., Ozel, T., Elias, J. S., Costentin, C. & Nocera, D. G. Interplay of homogeneous reactions, mass transport, and kinetics in determining selectivity of the reduction of CO2 on gold electrodes. *ACS Cent Sci* **5**, 1097–1105 (2019).

[5] Dunwell, M., Luc, W., Yan, Y., Jiao, F. & Xu, B. Understanding Surface-Mediated electrochemical reactions: CO2 reduction and beyond. *ACS Catal.* **8**, 8121–8129 (2018).

[6] Dunwell, M. *et al.* The central role of bicarbonate in the electrochemical reduction of carbon dioxide on gold. *J. Am. Chem. Soc.* **139**, 3774–3783 (2017).

[7] Chen, L. D., Urushihara, M., Chan, K. & Nørskov, J. K. Electric Field Effects in Electrochemical CO2 Reduction. *ACS Catal.* **6**, 7133–7139 (2016).

[8] Singh, M. R., Goodpaster, J. D., Weber, A. Z., Head-Gordon, M. & Bell, A. T. Mechanistic insights into electrochemical reduction of CO2 over ag using density functional theory and transport models. *Proc. Natl. Acad. Sci. U. S. A.* **114**, E8812–E8821 (2017).

[9]Hansen, H. A., Varley, J. B., Peterson, A. A. & Nørskov, J. K. Understanding trends in the electrocatalytic activity of metals and enzymes for CO2 reduction to CO. *J. Phys. Chem. Lett.* **4**, 388–392 (2013).

[10]Bagger, A., Ju, W., Varela, A. S., Strasser, P. & Rossmeisl, J. Electrochemical CO2 reduction: A classification problem. *Chemphyschem* **18**, 3266–3273 (2017).

[11]Bagger, A., Arnarson, L., Hansen, M. H., Spohr, E. & Rossmeisl, J. Electrochemical CO reduction: A property of the electrochemical interface. *J. Am. Chem. Soc.* (2019).

[12]Gupta, N., Gattrell, M. & MacDougall, B. Calculation for the cathode surface concentrations in the electrochemical reduction of CO2 in KHCO3 solutions. *J. Appl. Electrochem.* **36**, 161–172 (2006).

[13]Varela, A. S., Kroschel, M., Reier, T. & Strasser, P. Controlling the selectivity of CO2 electroreduction on copper: The effect of the electrolyte concentration and the importance of the local ph. *Catal. Today* **260**, 8–13 (2016).

[14]Dunwell, M. *et al.* Examination of Near-Electrode concentration gradients and kinetic impacts on the electrochemical reduction of CO2 using Surface-Enhanced infrared spectroscopy. *ACS Catal.* 3999–4008 (2018).

[15]Ryu, J., Wuttig, A. & Surendranath, Y. Quantification of interfacial ph variation at molecular length scales using a concurrent Non-Faradaic reaction. *Angew. Chem. Int. Ed Engl.* **57**, 9300–9304 (2018).

[16]Suter, S. & Haussener, S. Optimizing mesostructured silver catalysts for selective carbon dioxide conversion into fuels. *Energy Environ. Sci.* **12**, 1668–1678 (2019).

[17]Sandberg, R. B., Montoya, J. H., Chan, K. & Nørskov, J. K. CO-CO coupling on cu facets: Coverage, strain and field effects. *Surf. Sci.* **654**, 56–62 (2016).

[18]Resasco, J. *et al.* Promoter Effects of Alkali Metal Cations on the Electrochemical Reduction of Carbon Dioxide. *J. Am. Chem. Soc.* **139**, 11277–11287 (2017).

[19]Clark, E. L. *et al.* Influence of atomic surface structure on the activity of ag for the electrochemical reduction of CO2 to CO. *ACS Catal.* (2019).

[20]Ringe, S. *et al.* Understanding cation effects in electrochemical CO2 reduction. *Energy Environ. Sci.* (2019).

[21]Varela, A. S. *et al.* ph effects on the selectivity of the electrocatalytic CO2 reduction on Graphene-Embedded Fe–N–C motifs: Bridging concepts between molecular homogeneous and Solid-State heterogeneous catalysis. *ACS Energy Lett.* 812–817 (2018).

[22]Liu, M. *et al.* Enhanced electrocatalytic CO_2 reduction via field-induced reagent concentration. *Nature* **537**, 382–386 (2016).

[23]Todoroki, N. *et al.* Surface atomic arrangement dependence of electrochemical CO2 reduction on gold: Online electrochemical mass spectrometric study on Low-Index au(hkl) surfaces. *ACS Catal.* 1383–1388 (2019).

[24]Gauthier, J. *et al.* Facile electron transfer to co_2 during adsorption at the metal — solution interface. Preprint at https://chemrxiv.org/ (2019).

[25]Peterson, A. A. Global optimization of Adsorbate–Surface structures while preserving molecular identity. *Top. Catal.* **57**, 40–53 (2014).

[26]Shi, C., Hansen, H. A., Lausche, A. C. & Nørskov, J. K. Trends in electrochemical CO2 reduction activity for open and close-packed metal surfaces. *Phys. Chem. Chem. Phys.* **16**, 4720–4727 (2014).

[27]Katayama, Y. *et al.* An in situ Surface-Enhanced infrared absorption spectroscopy study of electrochemical CO2 reduction: Selectivity dependence on surface C-Bound and O-Bound reaction intermediates. *J. Phys. Chem. C* (2018).

[28]Strmcnik, D., Lopes, P. P., Genorio, B., Stamenkovic, V. R. & Markovic, N. M. Design principles for hydrogen evolution reaction catalyst materials. *Nano Energy* **29**, 29–36 (2016).

[29]Ooka, H., Figueiredo, M. C. & Koper, M. T. M. Competition between hydrogen evolution and carbon dioxide reduction on copper electrodes in mildly acidic media. *Langmuir* **33**, 9307–9313 (2017).

[30]Bigeleisen, J. The relative reaction velocities of isotopic molecules. *J. Chem. Phys.* **17**, 675–678 (1949).

[31]Robinson, R. A., Paabo, M. & Bates, R. G. Deuterium isotope effect on the dissociation of weak acids in water and deuterium oxide. *J. Res. Natl. Bur. Stand.* (1969).

[32]Nørskov, J. K. *et al.* Origin of the overpotential for oxygen reduction at a Fuel-Cell cathode. *J. Phys. Chem. B* **108**, 17886–17892 (2004).

[33]Chan, K. & Nørskov, J. K. Potential dependence of electrochemical barriers from ab initio calculations. *J. Phys. Chem. Lett.* **7**, 1686–1690 (2016).

[34]Mezzavilla, S., Horch, S., Stephens, I. E. L., Seger, B. & Chorkendorff, I. Structure sensitivity in the electrocatalytic reduction of CO2 with gold catalysts. *Angew. Chem. Int. Ed Engl.* (2019).

[35]Mariano, R. G., McKelvey, K., White, H. S. & Kanan, M. W. Selective increase in CO2 electroreduction activity at grain-boundary surface terminations. *Science* **358**, 1187–1192 (2017).

[36]Hori, Y., Murata, A., Kikuchi, K. & Suzuki, S. Electrochemical reduction of carbon dioxides to carbon monoxide at a gold electrode in aqueous potassium hydrogen carbonate. *J. Chem. Soc. Chem. Commun.* **0**, 728–729 (1987).

[37]Chen, Y., Li, C. W. & Kanan, M. W. Aqueous CO2 reduction at very low overpotential on oxide-derived au nanoparticles. *J. Am. Chem. Soc.* **134**, 19969–19972 (2012).

[38]Stegelmann, C., Andreasen, A. & Campbell, C. T. Degree of rate control: how much the energies of intermediates and transition states control rates. *J. Am. Chem. Soc.* **131**, 8077–8082 (2009).

[39]Shi, C., Chan, K., Yoo, J. S. & Nørskov, J. K. Barriers of Electrochemical CO2 Reduction on Transition Metals. *Org. Process Res. Dev.* **20**, 1424–1430 (2016).

[40]Wu, Y. *et al.* A Two-Dimensional MoS2 catalysis transistor by Solid-State ion gating manipulation and adjustment (SIGMA). *Nano Lett.* (2019).

[41]Liu, X. *et al.* ph effects on the electrochemical reduction of CO(2) towards C2 products on stepped copper. *Nat. Commun.* **10**, 32 (2019).

[42]Kuhl, K. P., Cave, E. R., Abram, D. N. & Jaramillo, T. F. New insights into the electrochemical reduction of carbon dioxide on metallic copper surfaces. *Energy Environ. Sci.* **5**, 7050–7059 (2012).

[43]Cave, E. R. *et al.* Electrochemical CO 2 reduction on au surfaces: mechanistic aspects regarding the formation of major and minor products. *Phys. Chem. Chem. Phys.* **19**, 15856–15863 (2017).

[44]Wang, L. *et al.* Electrochemical carbon monoxide reduction on polycrystalline copper: Effects of potential, pressure, and ph on selectivity toward multicarbon and oxygenated products. *ACS Catal.* **8**, 7445–7454 (2018).

[45]Morales-Guio, C. G. *et al.* Improved CO2 reduction activity towards c2+ alcohols on a tandem gold on copper electrocatalyst. *Nature Catalysis* **1**, 764–771 (2018).

[46]Frumkin, A. N. Influence of cation adsorption on the kinetics of electrode processes. *Trans. Faraday Soc.* **55**, 156–167 (1959).

[47]Nørskov, J. K., Studt, F., Abild-Pedersen, F. & Bligaard, T. *Fundamental Concepts in Heterogeneous Catalysis* (Wiley, 2014), 1 edition edn.

[48]Patel, A. M. *et al.* Theoretical approaches to describing the oxygen reduction reaction activity of Single-Atom catalysts. *J. Phys. Chem. C* **122**, 29307–29318 (2018).

[49]Gauthier, J. A. *et al.* Challenges in modeling electrochemical reaction energetics with polarizable continuum models. *ACS Catal.* **9**, 920–931 (2019).

[50]Jinnouchi, R. & Anderson, A. B. Electronic structure calculations of liquid-solid interfaces: Combination of density functional theory and modified Poisson-Boltzmann theory. *Phys. Rev. B Condens. Matter* **77**, 245417 (2008).

[51]Otani, M. & Sugino, O. First-principles calculations of charged surfaces and interfaces: A plane-wave nonrepeated slab approach. *Phys. Rev. B Condens. Matter* **73**, 115407 (2006).

[52]Gauthier, J., Dickens, C., Heenen, H. H., Ringe, S. & Chan, K.

Unified approach to implicit and explicit solvent simulations of electrochemical reaction energetics (2019).
[53] Gauthier, J., Dickens, C., Ringe, S. & Chan, K. Practical considerations for continuum models applied to surface electrochemistry (2019).
[54] Andreussi, O., Dabo, I. & Marzari, N. Revised self-consistent continuum solvation in electronic-structure calculations. *J. Chem. Phys.* **136**, 064102 (2012).
[55] Giannozzi, P. *et al.* QUANTUM ESPRESSO: a modular and open-source software project for quantum simulations of materials. *J. Phys. Condens. Matter* **21**, 395502 (2009).
[56] Parsons, R. The metal-liquid electrolyte interface. *Solid State Ionics* **94**, 91–98 (1997).
[57] MacGillivray, A. D. Nernst-Planck equations and the electroneutrality and donnan equilibrium assumptions. *J. Chem. Phys.* **48**, 2903–2907 (1968).
[58] Smith, C. P. & White, H. S. Theory of the voltammetric response of electrodes of submicron dimensions. violation of electroneutrality in the presence of excess supporting electrolyte. *Anal. Chem.* **65**, 3343–3353 (1993).
[59] Trasatti, S. & Lust, E. The potential of zero charge. In White, R. E. & J. O'M. Bockris, B. E. C. (eds.) *Modern Aspects of Electrochemistry*, vol. 33 (KluwerAcademic/PlenumPublishers, New York).
[60] Borukhov, I., Andelman, D. & Orland, H. Adsorption of large ions from an electrolyte solution: a modified Poisson–Boltzmann equation. *Electrochim. Acta* **46**, 221–229 (2000).
[61] Wang, H., Thiele, A. & Pilon, L. Simulations of cyclic voltammetry for electric double layers in asymmetric electrolytes: A generalized modified Poisson–Nernst–Planck model. *J. Phys. Chem. C* **117**, 18286–18297 (2013).
[62] Lucas, C. A., Thompson, P., Gründer, Y. & Markovic, N. M. The structure of the electrochemical double layer: Ag(111) in alkaline electrolyte. *Electrochem. commun.* **13**, 1205–1208 (2011).
[63] Chan, K. & Eikerling, M. A Pore-Scale model of oxygen reduction in Ionomer-Free catalyst layers of PEFCs. *J. Electrochem. Soc.* **158**, B18–B28 (2011).
[64] Ando, Y., Gohda, Y. & Tsuneyuki, S. Ab initio molecular dynamics study of the helmholtz layer formed on solid–liquid interfaces and its capacitance. *Chem. Phys. Lett.* **556**, 9–12 (2013).
[65] Sundararaman, R., Figueiredo, M. C., Koper, M. T. M. & Schwarz, K. A. Electrochemical capacitance of CO-Terminated pt(111) dominated by the CO-Solvent gap. *J. Phys. Chem. Lett.* **8**, 5344–5348 (2017).
[66] Amokrane, S. & Badiali, J. P. Analysis of the capacitance of the Metal-Solution interface: Role of the metal and the Metal-Solvent coupling. In White, R. E. & J. O'M. Bockris, B. E. C. (eds.) *Modern Aspects of Electrochemistry*, vol. 22, 1–95 (Butterworths, New York).
[67] Eberhardt, D., Santos, E. & Schmickler, W. Impedance studies of reconstructed and non-reconstructed gold single crystal surfaces. *J. Electroanal. Chem.* **419**, 23–31 (1996).
[68] Pajkossy, T., Wandlowski, T. & Kolb, D. M. Impedance aspects of anion adsorption on gold single crystal electrodes. *J. Electroanal. Chem.* **414**, 209–220 (1996).
[69] Bazant, M., Chu, K. & Bayly, B. Current-Voltage relations for electrochemical thin films. *SIAM J. Appl. Math.* **65**, 1463–1484 (2005).
[70] Hammes-Schiffer, S. & Soudackov, A. V. Proton-coupled electron transfer in solution, proteins, and electrochemistry. *J. Phys. Chem. B* **112**, 14108–14123 (2008).
[71] Biesheuvel, P. M., van Soestbergen, M. & Bazant, M. Z. Imposed currents in galvanic cells. *Electrochim. Acta* **54**, 4857–4871 (2009).

Acknowledgments

This material is based in part on work performed by the Joint Center for Artificial Photosynthesis, a DOE Energy Innovation Hub, supported through the Office of Science of the U.S. Department of Energy, under Award No. DE-SC0004993. This research used resources of the National Energy Research Scientific Computing Center, a DOE Office of Science User Facility supported by the Office of Science of the U.S. Department of Energy under Contract No. DE-AC02-05CH11231. This work was supported in part by a research grant (9455) from "VILLUM FONDEN". The work of C.G.M.-G. was partially supported by the Swiss National Science Foundation (grant number P400P2-180767).

Author contributions

K.C. conceived the initial research plan and ideas, L.C. and M.F. performed initial explicit water DFT simulations and S.R. continued the work using implicit solvent. S.R. together with K.C. developed the transport-corrected electrochemical model presented in this work with input from C.G.M.-G. S.R. developed and applied the mass transport package `CatINT` and the micro-kinetic and transport models. C.G.M-G. carried out the experimental CO_2 reduction experiments under the guidance of C.H. and T.F.J. All authors contributed to the discussion of the results, the manuscript was written by S.R. and K.C. with major contributions from C.G.M.-G. and all other authors.

Competing interests

The authors declare no competing interests.